Capturing the interactions in the BaSnF4 ionic conductor: Comparison between a machine-learning potential and a polarizable force field

Xiliang Lian, Mathieu Salanne

Accepted to J. Chem. Phys. 10.1063/5.0169343

Capturing the interactions in the $BaSnF_4$ ionic conductor: comparison between a machine-learning potential and a polarizable force field

Xiliang Lian[1, 2, a)] and Mathieu Salanne[1, 2, 3, b)]

[1)] *Sorbonne Université, CNRS, Physicochimie des Électrolytes et Nanosystèmes Interfaciaux, F-75005 Paris, France*

[2)] *Réseau sur le Stockage Electrochimique de l'Energie (RS2E), FR CNRS 3459, 80039 Amiens Cedex, France*

[3)] *Institut Universitaire de France (IUF), 75231 Paris, France*

(Dated: 20 September 2023)

$BaSnF_4$ is a prospective solid state electrolyte for fluoride ion batteries. However, the diffusion mechanism of the fluoride ions remains difficult to study, both in experiments and in simulations. In principle, ab initio molecular dynamics could allow to fill this gap, but this method remains very costly from the computational point of view. Using machine learning potentials is a promising method that can potentially address the the accuracy issues of classical empirical potentials while maintaining high efficiency. In this work, we fitted a dipole polarizable ion model and trained machine learning potential for $BaSnF_4$ and made comprehensive comparisons on the ease of training, accuracy and efficiency. We also compared the results with the case of a simpler ionic system (NaF). We show that contrarily to the latter, for $BaSnF_4$ the machine learning potential offers much higher versatility. The current work lays foundations for the investigation of fluoride ion mobility in $BaSnF_4$ and provides insight on the choice of methods for atomistic simulations.

[a)] xiliang.lian@sorbonne-universite.fr

[b)] mathieu.salanne@sorbonne-universite.fr

I. INTRODUCTION

Fluoride ion batteries (FIBs) are a promising alternative to Lithium-ion batteries due to their improved safety, low cost, and high theoretical volumetric energy density. They have therefore become increasingly investigated in recent years[1–3]. However, the low ionic mobility of fluoride ions within the solid electrolyte and the requirement of high-temperature operation are the main bottlenecks to overcome before a potential commercialization of FIBs[1]. The best performance in terms of ionic conductivity are obtained with $PbSnF_4$ that can reach as high as 1×10^{-3} S cm^{-1} at room temperature but its application is hampered by the fact that both Pb and Sn can be oxidized and Pb will pose environmental issues. Substituting Pb with Ba results in $BaSnF_4$ which exhibits reasonably high room temperature ionic conductivity, yet it remains far below that of Li-ion ionic conductors. The tetragonal phase of $BaSnF_4$ possesses ionic conductivity almost two orders of magnitude higher than the cubic one[4], and is of particular interest for solid-state electrolytes. The structure of tetragonal phase $BaSnF_4$ (simply referred as $BaSnF_4$ in the remaining of the text) is shown on Fig. 1 (a) and can be described as alternating Ba-Ba and Sn-Sn double layers. Notably, the Sn atoms have stereoactive lone pairs pointing towards the near-empty Sn-Sn layer[5]. Previous work using NMR technique has shown that two different fluoride ion sublattices exist[6]. The fluoride ions lying between the Ba-Ba layers are immobile and require high energy to migrate while the fluoride ions located between the Ba-Sn / Sn-Sn (the latter with fractional occupation, not shown in the figure) layers are highly mobile and are under rapid exchange even at room temperature. Interestingly, at high temperatures, the participation of fluoride ions between Ba-Ba layers to the conduction can be observed from the 2D NMR exchange spectra. Despite a few experimental and theoretical works on $BaSnF_4$, the ionic conduction mechanism between Ba-Sn/Sn-Sn layers is still unclear and understanding it would significantly benefit to the rational design of FIB electrolytes.

Modeling accurately the interactions in $BaSnF_4$ using computer simulations is challenging since the lone-pair interactions are tricky to capture and the relatively low ionic conductivity requires long molecular dynamics (MD) simulations. Density functional theory (DFT)-based *ab initio* molecular dynamics (AIMD) provides an accurate description of the interactions, but this method is limited to small system sizes and to trajectories of hundreds of picoseconds due to its high computational cost. Classical MD allows to obtain trajectories over much

longer time scales and has shown exceptional performance in numerous previous researches of ionic conductors. This is because it involves classical interaction potentials (IP) which are generally based on simple analytical expressions that try to mimic the physical phenomenon at play. In particular, previous works have proved the accuracy of polarizable models (the so-called dipole-polarizable ionic model (DIPPIM)) for simulating ionic materials,[7,8] and even ionic conductors such as PbF_2[9] or $Li_7La_3Zr_2O_{12}$[10]. However, the existence of Sn lone pairs is hard to account for when using such classical IP.

This limitation may be overcome by using data-driven approaches instead. In particular, machine learning potentials (MLPs), since the initial work by Behler and Parrinello, have received significant amount of attention[11–13]. They are expected to exhibit *ab initio* accuracy at a computational efficiency comparable to that of classical IPs. MLP describes the potential energy surface by establishing a statistical relationship between the energy and structures, which are described by descriptors in MLPs. These descriptors are constructed in such a way that the energy of a structure is invariant in translation, rotation and permutation of two chemically identical atoms. Previous work has shown that MLPs works well for simple systems such as Si, Ni, Cu etc.[14] and also provide accurate results for relatively complex materials such as $Li_7La_3Zr_2O_{12}$[15] and liquids such as molten NaCl[16]. The almost perfect agreement between MLP and DFT results reveals that MLP can capture the local environmental variations very well although the physical terms are not explicitly included. Although MLP has demonstrated excellent performance for CaF_2[17], there has not been significant work on MLP for fluoride ion conductors and it has so far not been applied to systems with delicate interactions as $BaSnF_4$.

In this work, we fitted classical IP and trained MLP for $BaSnF_4$. To make effective comparisons, we have included NaF as a reference system since it adopts a much simpler rocksalt structure (Fig. 1 (b)) for which the DIPPIM is expected to perform well. For both systems, the two methods are compared in terms of parameterization difficulty (i.e. the amount of necessary data in the parameterization process), computational cost, and accuracy for reproducing structural, thermodynamic and vibrational properties. We show that the versatility of MLPs makes them more adequate for simulating systems with complex interactions, despite a lower computational efficiency.

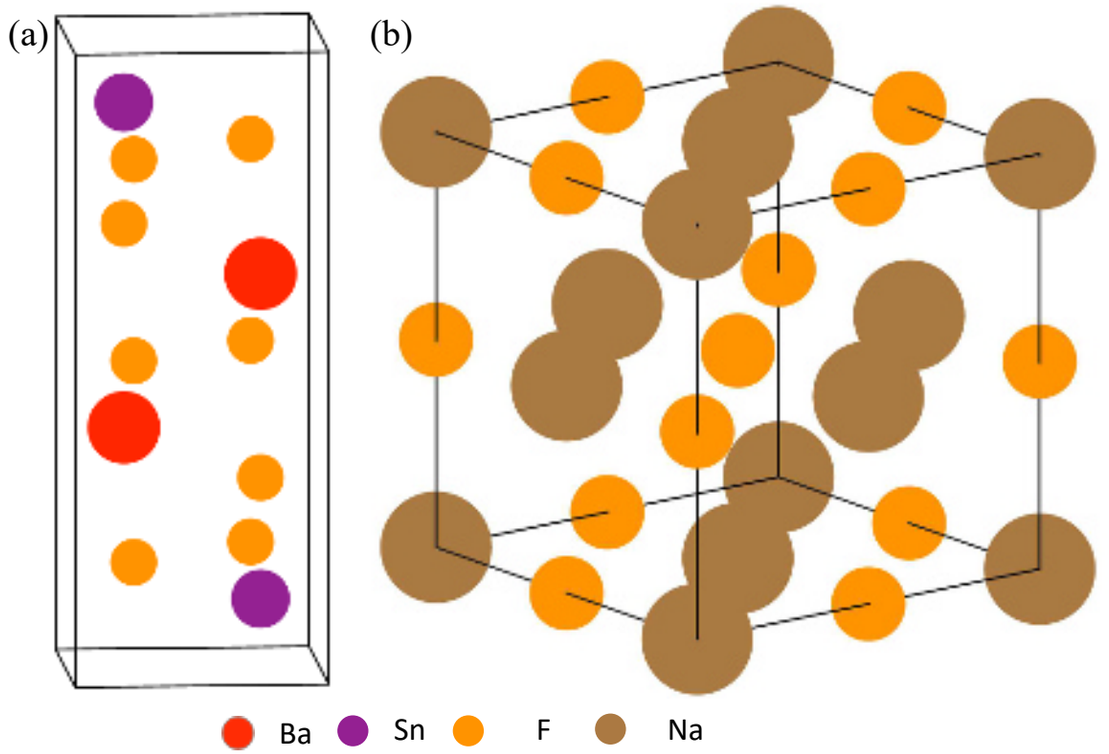

FIG. 1: (a) Crystal structure of $BaSnF_4$ (b) Crystal structure of NaF

II. COMPUTATIONAL METHODS

A. Ab initio Molecular Dynamics

AIMD simulations were conducted using the Vienna ab initio simulation package (VASP) within the density-functional theory (DFT) framework[18,19]. The electronic wave functions were expanded in a plane-wave basis set. The core-valence interactions are described by projector-augmented wave (PAW) pseudopotentials. For all the AIMD calculations, the Brillouin zone is sampled at gamma point only to increase the efficiency and the electronic convergence threshold is 10^{-6} eV. The Verlet algorithm is used to integrate Newton's equations of motion, at a time step of 1 fs on an NVT ensemble where we fix the number of atoms, the volume, and the temperature. Nosé-Hoover thermostat is used to control the temperature at 298 K. The same set of parameters were used when applying MLP.

For NaF, the exchange-correlation energy is approached with Perdew-Burke-Ernzerhof (PBE) functional[20] with a kinetic energy cutoff of 700 eV. The valence configuration for Na

and F are $2s^2 2p^6 3s^1$ and $2s^2 2p^5$. We took the initial configuration from materials project database[21] and the AIMD calculations are made with a 2×2×2 supercell. For $BaSnF_4$, the calculations are performed with PBE for solids (PBESol) exchange-correlation functional[22], which was found to best reproduce the experimental data as shown in the Supplementary Table I. The plane wave cutoff of $BaSnF_4$ was set to 520 eV. The valence shell configurations for Ba, Sn, and F are $5s^2 5p^6 6s^2$, $4d^{10} 5s^2 5p^2$, and $2s^2 2p^5$ respectively. The initial configuration is taken from the experiment and a 3×3×1 supercell is constructed for AIMD calculation.

B. Machine Learning Potential

1. Model

We employ on-the-fly MLPs following the methodology described and implemented in VASP to generate MLPs for $BaSnF_4$ and NaF. The underlying theory and training parameters are extensively described in the previous works[23,24]. In this context, we provide a succinct overview of the pertinent theoretical aspects employed in this study only.

The potential energy surface of a given structure with N atoms is decomposed into contributions from individual atomic energies:

$$U = \sum_{i=1}^{N} U_i$$

The local energy is determined by the local environments, which can be represented by the local atomic distribution:

$$\rho_i(r) = \sum_{j=1}^{N} f_{cut}(r_{ij}) g(r - r_{ij})$$

where f_{cut} is a cutoff function which excludes the contributions of environments outside the cutoff radius and $g(r - r_{ij})$ is a Gaussian-type delta function. In VASP implementation, radial ($\rho_i^{(2)}$) and angular descriptors ($\rho_i^{(3)}$) that can satisfy the rotational invariance are constructed to describe the local environments. Therefore, we have:

$$U_i = F[\rho_i^{(2)}, \rho_i^{(3)}]$$

The radial descriptor describes the probability of finding another atom j from the ith atom with a distance r. The angular descriptor in this context refers to the probability of

observing atom j at a distance r from atom i, and simultaneously observing atom k at a distance s from atom i, with an angle $\angle kij = \theta$ between them. In practice, the descriptors are discretized and expanded into terms of radial basis functions and spherical harmonics:

$$\rho_i^{(2)}(r) = \frac{1}{\sqrt{4\pi}} \sum_{n=1}^{N_R^0} c_n^i \chi_{n0}(r)$$

$$\rho_i^{(3)}(r,s,\theta) = \sum_{l=0}^{L_{max}} \sum_{n=1}^{N_R^l} \sum_{\mu=1}^{N_R^l} \sqrt{\frac{2l+1}{2}} p_{n\mu l}^i \chi_{nl}(r) \chi_{\mu l}(s) P_l(cos\theta)$$

and the expansion coefficients for angular descriptors are given in $P_{nl\mu}^i$:

$$P_{n\mu l}^i = \sqrt{\frac{8\pi^2}{2l+1}} \sum_{m=-l}^{l} [c_{nlm}^i c_{\mu lm}^{i*} - \sum_{j}^{N_a} c_{nlm}^{ij} c_{\mu lm}^{ij*}]$$

where $\chi_{\mu l}$ and P_l denote normalized spherical Bessel functions and Legendre polynomials of order l respectively. Here, c_{nlm}^i, N_R^0, and N_R^l respectively represent the expansion coefficients, number of radial basis functions for radial descriptors $\rho_i^{(2)}(r)$, and number of radial basis functions for angular descriptors $\rho_i^{(3)}(r)$. The indices n, l, m represent the radial, angular and magnetic quantum numbers. The descriptors are expressed as coefficients vectors in the MLP:

$$x_i^{(2)^T} = (c_1^i, c_2^i, ...)$$

$$x_i^{(3)^T} = (p_{110}^i, p_{111}^i, ..., p_{120}^i, p_{121}^i, ...)$$

Finally, the energy can be written as weighted kernel function $K(x_i, x_{iB})$ where x_i and x_{iB} respectively represent the local instantaneous and the local reference configurations:

$$F(x_i) = \sum_{i_B=1}^{N_B} \omega_{iB} K(x_i, x_{iB})$$

The kernel function takes the following form:

$$K(x_i, x_{iB}) = [\beta^{(2)}(x_i^{(2)} \cdot x_{iB}^{(2)}) + \beta^{(3)}(\hat{x}_i^{(3)} \cdot \hat{x}_{iB}^{(3)}))]^{\zeta^{(3)}}$$

Here, the $\hat{x}_i^{(3)}$ denotes a normalized vector of $x_i^{(3)}$. $\beta^{(2)}$ and $\beta^{(2)}$ are weighting parameters. $\zeta^{(3)}$ controls the sharpness of the kernel function.

2. *Training*

In this study, the MLP training process was performed on-the-fly, which involved constructing the potential during the AIMD calculations. The parameters for controlling the AIMD part of the calculations were set up as described in the previous section. Now, we provide a brief summary of the model training procedures and preliminary results.

To generate the MLP datasets for NaF, a 2×2×2 supercell containing 64 atoms was utilized. The initial structure was equilibrated at 300 K for 30 ps using AIMD before the training. Then, The ML model was trained by gradually heating the system from 250 K to 600 K, which allows for a broader sampling of the potential energy surface. In the case of $BaSnF_4$, a slightly different setup was employed. A 3×3×1 supercell consisting of 108 atoms was used, and the model was trained by gradually heating the system from 200 K to 500 K over 100 ps. The initial equilibration was performed at 298 K for 50 ps using the on-the-fly training scheme. Following this equilibration, the MLP was abandoned and the final configuration obtained from the equilibration step served as the starting point for further training.

Here, we discuss some important hyperparameters used across the training. The cutoff radius for radial $\rho_i^{(2)}(r)$ and angular descriptors $\rho_i^{(3)}(r)$ were set to 6 Å with a Gaussian broadening width of 0.5 Å. The number of spherical Bessel functions for radial (N_R^0) and angular descriptors (N_R^l) was set to 8 for both. L_{max}, the maximum value of the angular quantum number, was set to 4. The kernel function sharpness parameter $\zeta^{(3)}$ was set to 4. Ultimately, the algorithm sampled 244 and 516 reference structure datasets (from which the local reference configurations are extracted) for NaF and $BaSnF_4$ respectively. For NaF, 240 and 221 local reference configurations are selected for Na and F, indicating that Na and F local environments are equally complex. In the case of $BaSnF_4$, 130, 606, and 1388 local reference configurations for Ba, Sn, and F have been sampled by the code. Intuitively, the Ba atoms have the most symmetric environment, thus requiring a smaller amount of reference configurations to describe them. In the case of Sn atoms, the presence of stereoactive lone pairs pointing towards the Sn-Sn empty layer results in the need for more reference configurations. Finally, it is not surprising that we need the highest number of local reference configurations for fluoride ions since they sit in various crystallographic site with different cationic environment. In addition they are the conducting species inside the structure and

are highly mobile even at room temperature.

C. Classical Interaction Potential: DIPPIM

1. Model

The DIPPIM has been previously reported and successfully applied to the study of many ionic materials, including solid-state Li-ion batteries electrolytes[10] and fluoride ionic conductors. While interaction potentials were previously reported for NaF[25], they were generally aimed at simulating the molten state, so that in the current work we have fitted a new set of parameters to ensure its consistency with $BaSnF_4$, a system for which the interaction potential has never been previously reported. The DIPPIM comprises four components, including charge-charge interaction, short-range repulsion, dispersion interaction, and the dipolar interaction.

The coulombic or charge-charge interactions are defined by

$$V^{qq}(r_{ij}) = \sum_{i \leq j} \frac{q_i q_j}{r_{ij}}$$

where r_{ij} denotes the interatomic distances and q_i and q_j are charges carried by atoms i and j. The potential includes a short-range repulsive term with an exponential behavior within the interionic separation range. A Gaussian function is added as a steep repulsive wall to avoid unstabilities at high temperatures. This term is especially beneficial for systems with highly polarizable ions, like oxygen, as it prevents numerical instabilities in dipoles at very small anion-cation separations. Here, we have imposed the repulsive wall on Ba-F and Sn-F interactions. This short-range potential reads:

$$V^{rep}(r_{ij}) = \sum_{i \leq j} \frac{B_{ij} exp(-\eta_{ij} r_{ij})}{r_{ij}^n} + \sum_{i \leq j} B'_{ij} exp(-\eta'_{ij} r_{ij}^2)$$

The dispersion interactions include dipole-dipole and dipole-quadruple terms:

$$V^{disp}(r_{ij}) = -\sum_{i \leq j} \left[f_6^{ij}(r_{ij}) \frac{C_{ij}^6}{r_{ij}^6} + f_8^{ij}(r_{ij}) \frac{D_{ij}^8}{r_{ij}^8} \right]$$

where C_6^{ij} and D_8^{ij} are the dipole-dipole and dipole-quadruple dispersion coefficients. The Tang-Toennies functions[26] are used to damp the dispersion terms at short range:

$$f_n^{ij}(r_{ij}) = 1 - exp(-b_n^{ij} r_{ij}) \sum_{k=0}^{n} \frac{(b_n^{ij} r_{ij})^k}{k!}$$

Finally, the polarization part of the potential incorporates dipolar effects:

$$V^{pol}(r_{ij}) = \sum_{i,j} (q_i \mu_{j,\alpha} f_4^{ij}(r_{ij}) - q_j \mu_{i,\alpha} f_4^{ji}(r_{ij})) T_\alpha^{(1)}(\mathbf{r}_{ij}) - \sum_{i,j} \mu_{i,\alpha} \mu_{j,\beta} T_{\alpha\beta}^{(2)}(r_{ij}) + \sum_i \frac{1}{2\alpha_i} |\boldsymbol{\mu_i}|^2$$

In the above expression, α_i represents the polarizability of ion i, while $\boldsymbol{\mu}_i$ denotes the dipoles. Additionally, $\boldsymbol{T^{(1)}}$ and $\boldsymbol{T^{(2)}}$ correspond to the charge-dipole and dipole-dipole interaction tensors, respectively. The components of these tensors are given by:

$$T_\alpha^{(1)}(r_{ij}) = -r_\alpha / r^3$$

$$T_{\alpha\beta}^{(2)}(r_{ij}) = (3 r_\alpha r_\beta - r^2 \delta_{\alpha\beta}) / r^5$$

The influence of short-range induction effects on the dipoles is considered by utilizing the Tang-Toennies damping functions (f_4^{ij})[26]. These damping functions, similar to those employed for damping dispersion interactions, take into account the overlap of charge densities that affect the induced dipoles. The parameter b_n^{ij} determines the range over which this overlap has an impact. Furthermore, the damping of these induction effects necessitates the inclusion of an additional pre-exponential parameter, c_{ij}, which determines the strength of the ion's response to this phenomenon:

$$f_n^{ij}(r_{ij}) = 1 - c^{ij} exp(-b_n^{ij} r_{ij}) \sum_{k=0}^{n} \frac{(b_n^{ij} r_{ij})^k}{k!}$$

Note that in the DIPPIM, the induced dipoles are treated as a set of additional degrees of freedom, which are obtained by minimizing the energy at each timestep. This is formally equivalent to determining them self-consistently, so that the polarization interactions have a many-body character.

2. Fitting of the parameters and simulations details

The DIPPIM for NaF and $BaSnF_4$ was fitted using a generalized force-fitting method. Initially, 10 configurations were randomly selected from the AIMD trajectory, for which

DFT calculations were performed to compute the forces. In addition, Wannier90 code was utilized to identify the Wannier centers and calculate the dipoles on each atom[27]. Fitting those in addition to the individual forces allows to reduce the risk of error cancellations between the various parts of the potential[28]. It is important to note that in the DIPPIM, the atomic charges are not treated as adjustable parameters; they are taken as the nominal charges of the ions, i.e. +1 for Na^+, -1 for F^- and +2 for Ba^{2+} and Sn^{2+}. The fitting process is performed by minimizing the following objective function:

$$\chi^2 = \frac{\sum_i^N |\boldsymbol{A}_i^{DFT} - \boldsymbol{A}_i^{IP}|^2}{\sum_i^N |\boldsymbol{A}_i^{DFT}|^2}$$

Here, $\mathbf{A}_i^{DFT}$ and $\mathbf{A}_i^{IP}$ comprise of the forces and dipoles for all atoms obtained from DFT calculations and the fitted interaction potential, respectively. For NaF and $BaSnF_4$, the resulting objective function values were found to be 0.003 and 0.23, respectively. In the case of $BaSnF_4$, the objective function could not be further reduced primarily due to the stability of the interaction potential.

All our calculations made with DIPPIM have been performed using Metalwalls[29,30]. The room temperature is maintained by a Nosé-Hoover chain thermostat with a characteristic period of 1 ps. Apart from this, the parameters are set to the same as those in AIMD calculations to ensure consistency.

III. RESULTS AND DISCUSSION

A. Validation of the potentials on DFT forces

To validate the two different methods on a similar dataset, we randomly select 200 structures from an independent molecular dynamics trajectory, ensuring that these configurations have not been encountered during the training/fitting process. The validation procedure involves comparing the computed energies, forces, and stresses from the MLPs with the corresponding values obtained from DFT. The validation of DIPPIM undergoes a similar validation process, with the comparison primarily focused on the agreement of forces, given the use of different codes for DFT (MLPs) and classical potentials.

The results presented in FIG. 2 (a) and (b) demonstrate the agreement between the DIPPIM and the MLP with the DFT results in the case of NaF. The bins color intensities

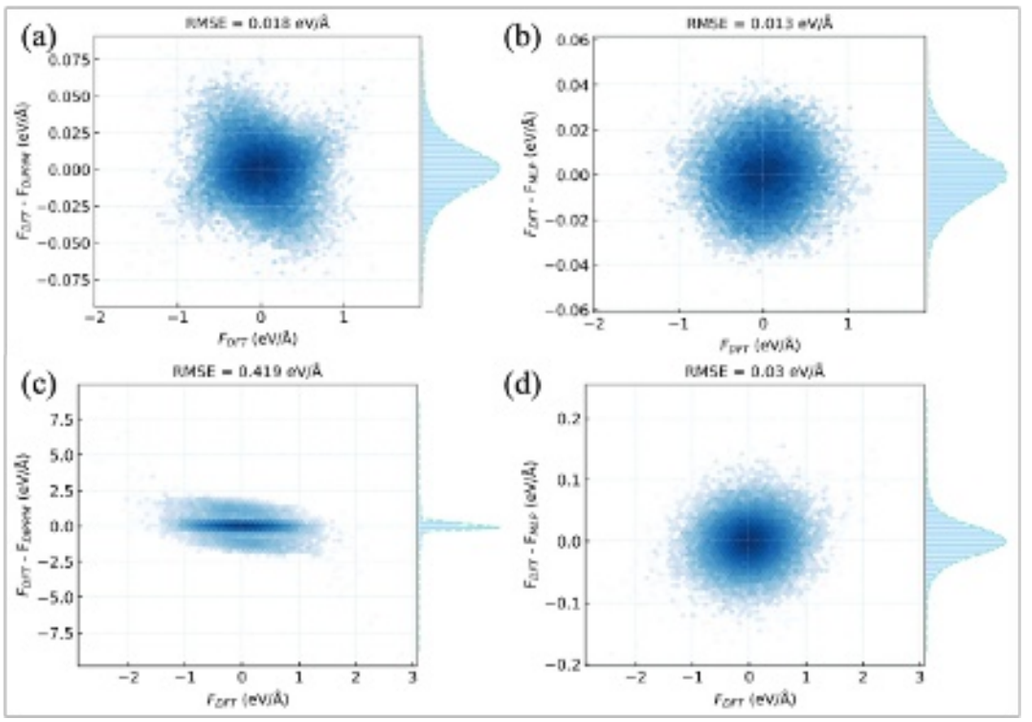

FIG. 2: (a)NaF forces comparison between DFT and DIPPIM. (b)NaF forces comparison between DFT and MLP. (c)$BaSnF_4$ forces comparison between DFT and DIPPIM. (d) $BaSnF_4$ forces comparison between DFT and MLP.

are proportional to the number of data points. In the case of MLP, the histogram displays a highly Gaussian distribution of the errors, showing that the errors are random. For DIPPIM, some deviations from Gaussian behavior are observed for the atoms with large absolute value of the DFT forces, which reflects the fact that the model does not fully catch the electronic structure effects. In terms of absolute error, the comparison of the root mean squared error (RMSE) reveals that the MLP slightly outperforms the DIPPIM.

In the case of $BaSnF_4$, we observe much more pronounced differences between MLP and DIPPIM. Firstly, the RMSE for the DIPPIM is nearly 14 times higher compared to that of the MLP. This higher RMSE for $BaSnF_4$ compared to NaF results from the presence of more complex local environments in $BaSnF_4$, necessitating a more sophisticated and adaptable approach, which the MLP effectively addresses. Secondly, we observe that the distribution of errors for the DIPPIM presents some systematic errors, with a strong deviation from a Gaussian behavior, which means that some important interactions are missed during the fitting process.

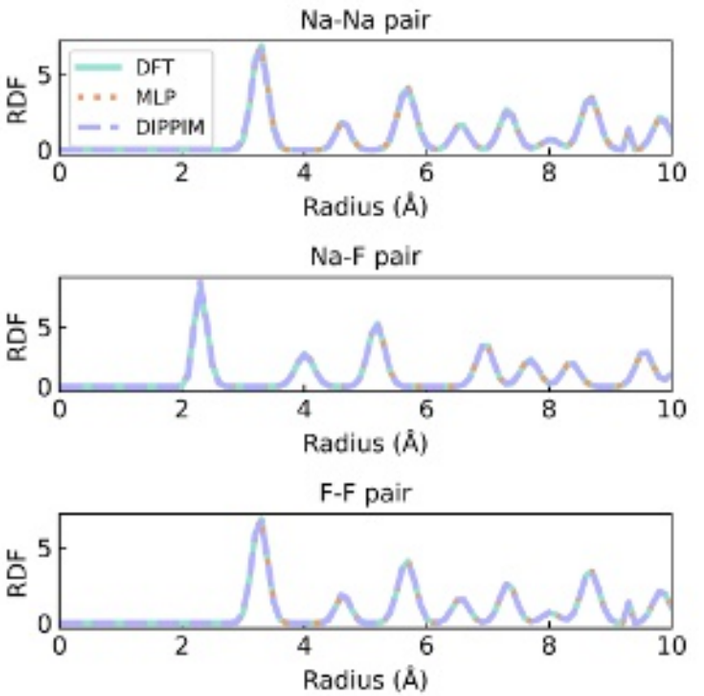

FIG. 3: Partial RDFs obtained at 298 K for NaF with AIMD (cyan, solid), DIPPIM (purple, dashed) and MLP (orange, dotted)

B. Structure of the materials

Despite the largest errors observed for the prediction of $BaSnF_4$ forces by the DIPPIM, it is useful to compare the two potentials for structural and vibrational properties: Classical IPs often remain predictive thanks to cancellation of errors between the various terms. In order to characterize the structure of the crystals at finite temperature, we calculated the radial distribution functions (RDFs) of NaF and $BaSnF_4$. FIG. 3 displays the partial RDFs obtained from the MLP, DIPPIM, and AIMD simulations for NaF. It is evident that the two effective potentials yield a structure in good agreement with that obtained from the DFT calculations.

However, for $BaSnF_4$, we observe more significant differences as shown in FIG. 4. Although the position of the first peaks, and thus the interatomic distances, are well caught by the DIPPIM, this model is not able to reproduce well the shape in various cases. Notably, in the Sn-Sn RDF around 4 Å, the DIPPIM fails to capture the peak splitting. We attribute this discrepancy to the presence of stereoactive Sn lone pairs. The intensity and the shape

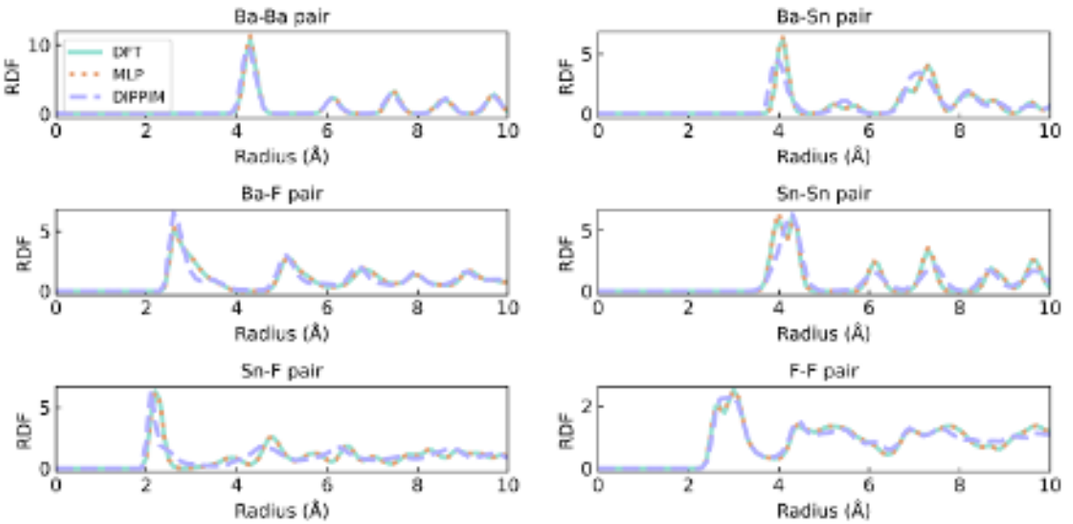

FIG. 4: Partial RDFs obtained at 298 K for $BaSnF_4$ with AIMD (cyan, solid), DIPPIM (purple, dashed) and MLP (orange, dotted)

of the Ba-F and Ba-Sn first peaks are also not very well reproduced, contrarily to the case of the MLP for which the agreement with DFT is almost quantitative. In conclusion, The DIPPIM model fails to account for the local environments of the atoms, whereas MLP showcases enhanced versatility despite lacking an explicit representation of the Sn lone pairs.

C. Vibrational properties

In the following section, we further compared the capability of MLPs and DIPPIMs to predict the vibrational properties of the materials by calculating the power spectrum and the phonon dispersion relations.

Power spectrum can be used to determine vibrational-rotational normal modes, or the vibrational density of states (VDOS) probed by experimental techniques such as infrared and Raman spectroscopies[31]. The VDOS is calculated by taking the Fourier transform of velocity autocorrelation function[32].

$$VDOS(\omega) = m \int < \boldsymbol{\nu}(\tau)\boldsymbol{\nu}(t+\tau) >_\tau e^{-i\omega t} dt$$

FIG. 5 and FIG. 6 show the simulated mass-weighted power spectrum for NaF and $BaSnF_4$, respectively. The power spectrum is calculated based on a separate 20 ps trajectory to ensure the convergence. For NaF, both DIPPIM and MLP can capture the normal nodes

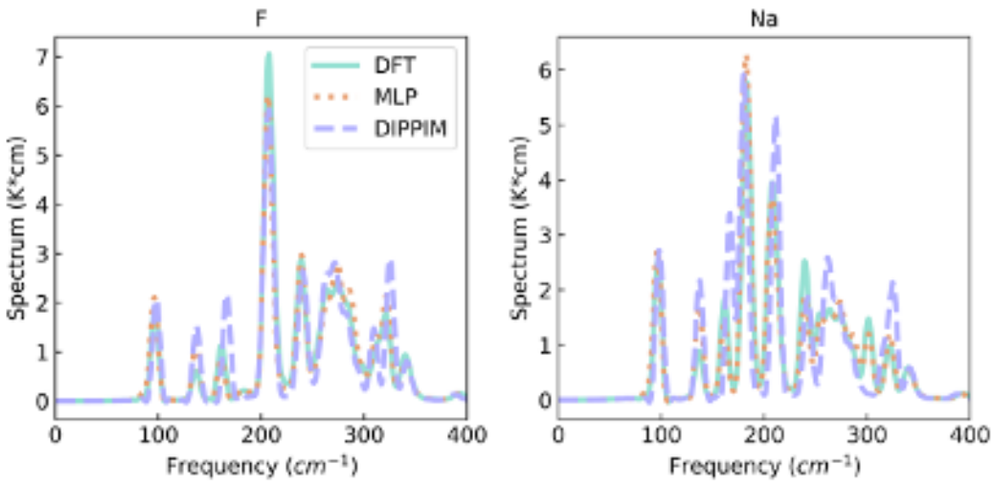

FIG. 5: NaF mass-weighted power spectrum computed using AIMD (cyan, solid), DIPPIM (purple, dashed) and MLP (orange, dotted)

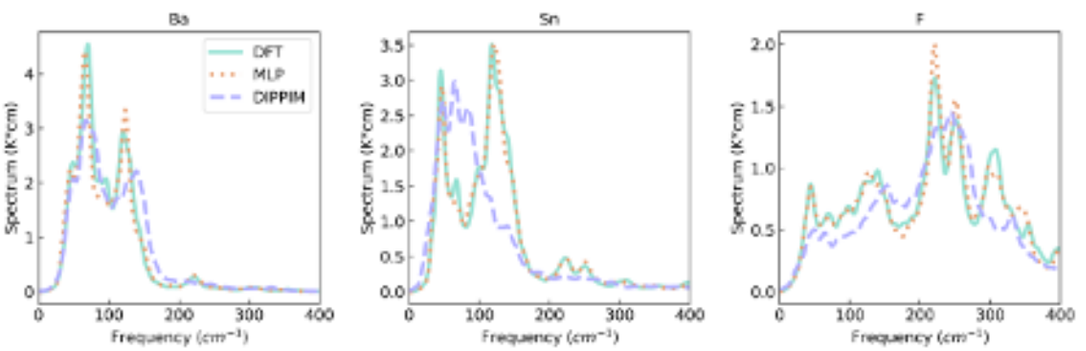

FIG. 6: $BaSnF_4$ mass-weighted power spectrum computed using DFT (cyan, solid), DIPPIM (purple, dashed) and MLP (orange, dotted)

reasonably well in comparison to the AIMD results. However, the peak intensities and positions predicted using DIPPIM show some slight deviations from the reference spectrum. As for the structure, the differences become more significant in the case of $BaSnF_4$. Unlike MLP potential, which is still capable of reproducing the peak positions and intensities, the DIPPIM almost fails to reproduce the DFT results. Specifically, in the Sn power spectra, there are two major peaks below and above 100 cm^{-1}. However, in the spectra obtained from DIPPIM, the peak above 100 cm^{-1} is almost missing and the peak below 100 cm^{-1} also shifts towards higher frequency. The failure shows the deficiency of DIPPIM to model the vibrational properties for $BaSnF_4$.

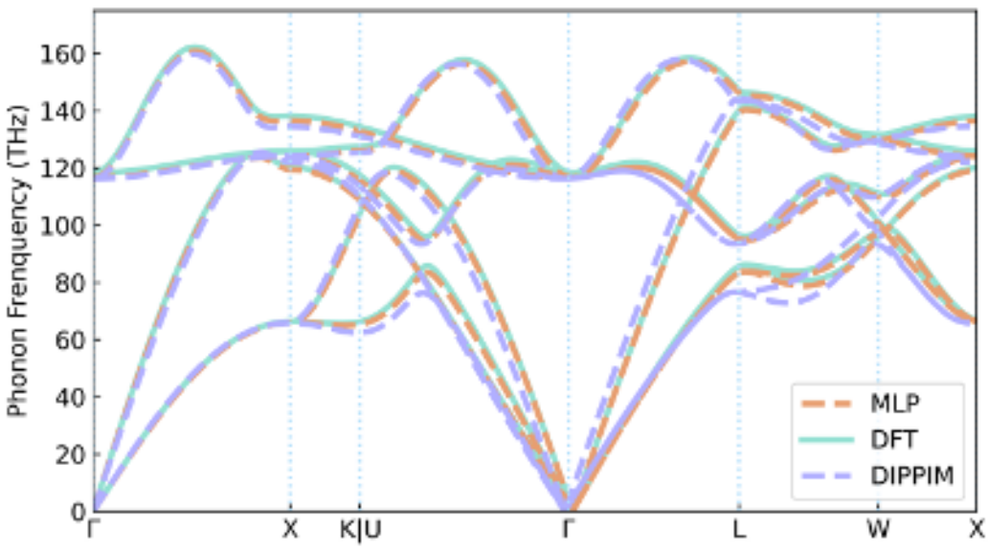

FIG. 7: Phonon dispersion of NaF obtained using DFT (cyan, solid), DIPPIM (purple, dashed) and MLP (orange, dotted)-based calculations

To go further, the phonon description is critical to understand the vibrational dynamics of a material and closely related to various thermal transport properties such as the thermal conductivity. We calculated the phonon dispersion of NaF with the same supercell as we did for our MLP training and DIPPIM fitting. The phonon dispersion results shown in FIG. 7 utilized the finite displacement method as implemented in Phonopy code[33,34]. We can see that both methods agree well with the result from DFT.

On the other hand, the phonon dispersion undoubtedly demonstrates the superiority of MLP when applied to $BaSnF_4$ as shown in FIG. 8 . While the MLP phonon dispersion does not perfectly match that of DFT, it qualitatively captures the essential features. As for NaF, we calculated the phonon dispersion using a supercell of the same size to reproduce the DFT results. As we can see the phonon frequency from DIPPIM significantly differs from that of DFT. Note that the existence of imaginary modes in $BaSnF_4$ indicates that this structure is unstable at 0 K. This is consistent with experiments since it has been shown that the tetragonal phase of $BaSnF_4$ occurs upon annealing at 460 K[4].

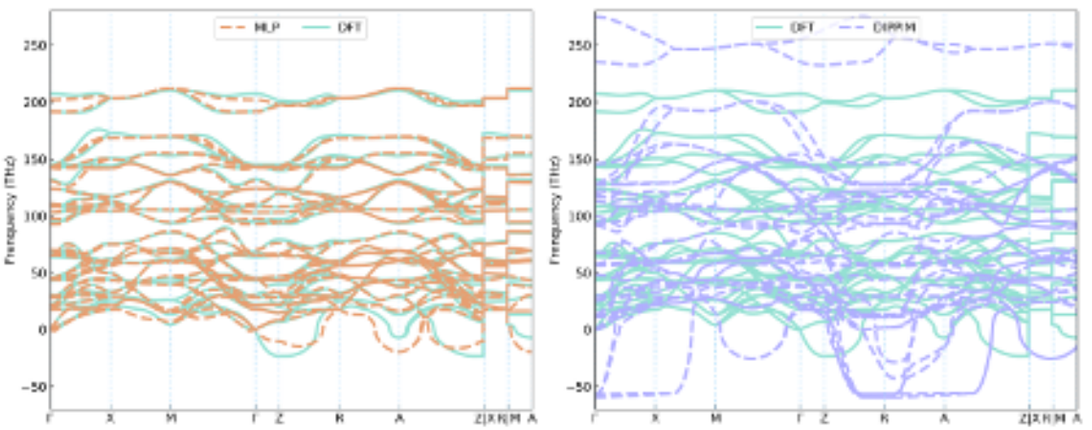

FIG. 8: (a) Phonon dispersion of $BaSnF_4$ obtained using DFT (cyan, solid) and MLP (orange, dotted)-based calculations. (b)Phonon dispersion of $BaSnF_4$ obtained using DFT (cyan, solid) and DIPPIM (purple, dashed)-based calculations.

D. Equation of state

Finally, in order to test the transferability of the potentials within a range of physical conditions not encountered during the training/fitting procedure, we computed the 0 K equation of state (EOS) of NaF and $BaSnF_4$. The EOS describes the material behavior under varied pressure and are of critical importance to the development and application of materials[35]. As shown in FIG. 9, we strained the volume from -10% $\sim$ 10% and plotted the normalized energies with respect to the volume. Next, we fitted the energy-volume relationship to Birch–Murnaghan equation of state[36,37] and the fitted modulus of NaF is 44.70 GPa, 55.30 GPa and 55.83 GPa respectively for DFT, MLP and DIPPIM. In the case of $BaSnF_4$, we obtained the following bulk modulus for DFT, MLP and DIPPIM: 68.89 GPa, 62.61 GPa and 115.58 GPa. The MLP computed bulk modulus deviates by 23.7% and 9.1% for NaF and $BaSnF_4$ from the DFT computed one, which can be ascribed to the fact that MLP has not been trained at various volumes. When pressure is close to zero, we have a nearly perfect agreement, which is reasonable because the thermodynamic condition is the same. For DIPPIM, the deviations of 24.8% and 67.8% are both larger than that of MLP, albeit the difference is almost negligible in the case of NaF. It is worth noting that the DIPPIM computed bulk modulus is astonishingly larger for $BaSnF_4$, which again confirmed the failure of this potential in correctly describing potential energy surface of $BaSnF_4$.

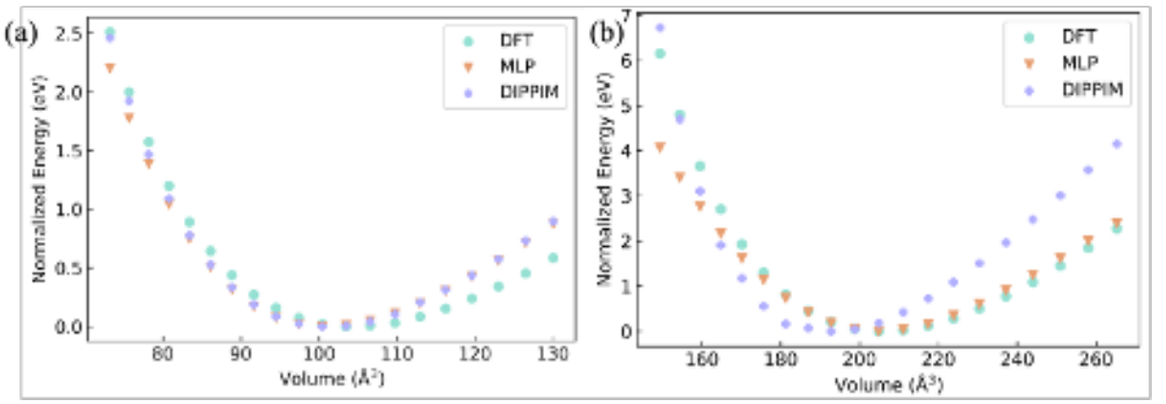

FIG. 9: (a) EOS of NaF as obtained with DFT (cyan, circle), MLP (orange, triangle), and DIPPIM (purple, cross). (b) EOS of $BaSnF_4$ as obtained with DFT (cyan, circle),DIPPIM (purple, cross and MLP (orange, triangle))

TABLE I: Computational cost for typical simulations performed with the MLP and DIPPIM

	number of atoms	number of nodes	MLP (s/step)	DIPPIM (s/step)
NaF	1728	2	0.4907	0.0448
$BaSnF_4$	600	3	0.3782	0.0285

E. Computational performances

It is worthwhile to mention the efficiency of the two interaction potentials. Typical timings are shown in Table. I. The calculations are performed on French supercomputer Jean-Zay where each node comprises of 40 cores[38]. The current efficiency tests for MLP were performed with the CPU compiled 6.3.2 version of VASP although the newer version is claimed to have significantly boosted efficiency. The efficiency tests for DIPPIM were performed with MetalWalls, compiled on CPU as well. We can see that in general, the DIPPIM is more than 10 times more efficient than MLP. Therefore, from the computational point of view, DIPPIM remains the solution of choice for systems for which it is accurate, i.e. in the absence of specific interactions, while for more complex materials such as $BaSnF_4$, the accuracy gain makes MLP a better choice than classical IP.

IV. SUMMARY

In summary, we have trained MLP and fitted DIPPIM for both NaF and $BaSnF_4$. In all the cases, the parameterization was made based on *ab initio* calculations only, i.e. no experimental information was used during this process. As a first accuracy test, we compared the forces computed from MLP and DIPPIM to those from DFT on the same set of configurations. Although the error made by the two models is similar in the case of NaF, the distribution of errors has a much more Gaussian behavior in the case of MLP, which tends to show that the DIPPIM fails to capture some of the interactions. The difference is much more pronounced in the case of $BaSnF_4$ due to the lack of a term to represent the stereoactive lone pairs of Sn in the DIPPIM.

To further compare the two methods, we computed a series of structural (RDF), vibrational (power spectrum, phonon dispersion) and thermodynamic (EOS) observables. In all cases, the results demonstrate that our trained MLPs for both are robust and versatile. We also conclude that for simple systems like NaF, classical IP is sufficient to model the system and give accurate representation of the potential energy surface at high efficiency. While for materials with more sophisticated interactions as in $BaSnF_4$, it is evident that fitting the interaction potential fails to provide a correct description of the system and using MLP is more advantageous.

SUPPLEMENTARY MATERIAL

The supplementary material contains the structural parameters obtained from geometry optimization using different functionals, the DIPPIM parameters for NaF and $BaSnF_4$ and a summary of the convergence test for the DIPPIM fitting for $BaSnF_4$.

ACKNOWLEDGMENTS

This work was granted access to the HPC resources of CINES under Allocation A0140910463 made by GENCI.

DATA AVAILABILITY

The data that support the findings of this study (input files for the simulations, raw data used for the various figures) are available on Zenodo (http://dx.doi.org/10.5281/zenodo.8354419).

REFERENCES

[1]A. W. Xiao, G. Galatolo, and M. Pasta, "The case for fluoride-ion batteries," Joule **5**, 2823–2844 (2021).

[2]M. A. Nowroozi, I. Mohammad, P. Molaiyan, K. Wissel, A. R. Munnangi, and O. Clemens, "Fluoride ion batteries – past, present, and future," Journal of Materials Chemistry A **9**, 5980–6012 (2021).

[3]Q. Liu, Y. Wang, X. Yang, D. Zhou, X. Wang, P. Jaumaux, F. Kang, B. Li, X. Ji, and G. Wang, "Rechargeable anion-shuttle batteries for low-cost energy storage," Chem **7**, 1993–2021 (2021).

[4]M. M. Ahmad, Y. Yamane, and K. Yamada, "Structure, ionic conduction, and giant dielectric properties of mechanochemically synthesized $BaSnF_4$," Journal of Applied Physics **106**, 074106 (2009).

[5]G. Dénès, T. Birchall, M. Sayer, and M. F. Bell, "$BaSnF_4$ — A new fluoride ionic conductor with the α-$PbSnF_4$ structure," Solid State Ionics **13**, 213–219 (1984).

[6]S. Chaudhuri, F. Wang, and CP Grey, "Resolving the different dynamics of the fluorine sublattices in the anionic conductor $BaSnF_4$ by using high-resolution MAS NMR techniques," Journal of The American Chemical Society **124**, 11746–11757 (2002).

[7]P. A. Madden, R. J. Heaton, A. Aguado, and S. Jahn, "From first-principles to material properties," Journal of Molecular Structure: THEOCHEM **771**, 9–18 (2006).

[8]M. Salanne and P. A. Madden, "Polarization effects in ionic solids and melts," Molecular Physics **109**, 2299–2315 (2011).

[9]M. J. Castiglione and P. A. Madden, "Fluoride ion disorder and clustering in superionic PbF_2," Journal of Physics: Condensed Matter **13**, 9963 (2001).

[10]M. Burbano, D. Carlier, F. Boucher, B. J. Morgan, and M. Salanne, "Sparse cyclic excitations explain the low ionic conductivity of stoichiometric $Li_7La_3Zr_2O_{12}$," Physical Review Letters **116**, 135901 (2016).

[11]J. Behler and M. Parrinello, "Generalized Neural-Network Representation of High-Dimensional Potential-Energy Surfaces," Physical Review Letters **98**, 146401 (2007).

[12]J. Behler, "Perspective: Machine learning potentials for atomistic simulations," The Journal of Chemical Physics **145**, 170901 (2016).

[13]O. T. Unke, S. Chmiela, H. E. Sauceda, M. Gastegger, I. Poltavsky, K. T. Schütt, A. Tkatchenko, and K.-R. Müller, "Machine Learning Force Fields," Chemical Reviews **121**, 10142–10186 (2021).

[14]Y. Zuo, C. Chen, X. Li, Z. Deng, Y. Chen, J. Behler, G. Csányi, A. V. Shapeev, A. P. Thompson, M. A. Wood, and S. P. Ong, "Performance and Cost Assessment of Machine Learning Interatomic Potentials," The Journal of Physical Chemistry A **124**, 731–745 (2020).

[15]K. Kim, A. Dive, A. Grieder, N. Adelstein, S. Kang, L. F. Wan, and B. C. Wood, "Flexible machine-learning interatomic potential for simulating structural disordering behavior of $Li_7La_3Zr_2O_{12}$ solid electrolytes," The Journal of Chemical Physics **156**, 221101 (2022).

[16]Q. J. Li, E. Küçükbenli, S. Lam, B. Khaykovich, E. Kaxiras, and J. Li, "Development of robust neural-network interatomic potential for molten salt," Cell Reports Physical Science **2**, 100359 (2021).

[17]S. Faraji, S. A. Ghasemi, S. Rostami, R. Rasoulkhani, B. Schaefer, S. Goedecker, and M. Amsler, "High accuracy and transferability of a neural network potential through charge equilibration for calcium fluoride," Physical Review B **95**, 104105 (2017).

[18]G. Kresse and J. Furthmüller, "Efficient iterative schemes for ab initio total-energy calculations using a plane-wave basis set," Physical Review B **54**, 11169–11169 (1996).

[19]G. Kresse and D. Joubert, "From ultrasoft pseudopotentials to the projector augmented-wave method," Physical Review B **59**, 1758–1758 (1999).

[20]J. P. Perdew, K. Burke, and M. Ernzerhof, "Generalized Gradient Approximation Made Simple," Physical Review Letters **77**, 3865–3865 (1996).

[21]A. Jain, S. P. Ong, G. Hautier, W. Chen, W. D. Richards, S. Dacek, S. Cholia, D. Gunter, D. Skinner, G. Ceder, and K. A. Persson, "Commentary: The materials project: A materials genome approach to accelerating materials innovation," APL Materials **1**, 011002 (2013).

[22]J. P. Perdew, A. Ruzsinszky, G. I. Csonka, O. A. Vydrov, G. E. Scuseria, L. A. Constantin, X. Zhou, and K. Burke, "Restoring the density-gradient expansion for exchange in solids

and surfaces," Physical Review Letters **100**, 136406–136406 (2008).

[23]R. Jinnouchi, F. Karsai, and G. Kresse, "On-the-fly machine learning force field generation: Application to melting points," Physical Review B **100**, 014105 (2019).

[24]R. Jinnouchi, J. Lahnsteiner, F. Karsai, G. Kresse, and M. Bokdam, "Phase Transitions of Hybrid Perovskites Simulated by Machine-Learning Force Fields Trained on the Fly with Bayesian Inference," Physical Review Letters **122**, 225701 (2019).

[25]M. Salanne, C. Simon, P. Turq, and P. A. Madden, "Heat-transport properties of molten fluorides: Determination from first-principles," Journal of Fluorine Chemistry Fluorine & Nuclear Energy, **130**, 38–44 (2009).

[26]K. T. Tang and J. P. Toennies, "An improved simple model for the van der Waals potential based on universal damping functions for the dispersion coefficients," The Journal of Chemical Physics **80**, 3726–3741 (1984).

[27]G. Pizzi, V. Vitale, R. Arita, S. Blügel, F. Freimuth, G. Géranton, M. Gibertini, D. Gresch, C. Johnson, T. Koretsune, J. Ibañez-Azpiroz, H. Lee, J.-M. Lihm, D. Marchand, A. Marrazzo, Y. Mokrousov, J. I. Mustafa, Y. Nohara, Y. Nomura, L. Paulatto, S. Poncé, T. Ponweiser, J. Qiao, F. Thöle, S. S. Tsirkin, M. Wierzbowska, N. Marzari, D. Vanderbilt, I. Souza, A. A. Mostofi, and J. R. Yates, "Wannier90 as a community code: New features and applications," Journal of Physics: Condensed Matter **32**, 165902 (2020).

[28]A. Aguado, L. Bernasconi, S. Jahn, and P. A. Madden, "Multipoles and interaction potentials in ionic materials from planewave-DFT calculations," Faraday Discussions **124**, 171–184 (2003).

[29]A. Marin-Laflèche, M. Haefele, L. Scalfi, A. Coretti, T. Dufils, G. Jeanmairet, S. K. Reed, S. Alessandra, R. Berthin, C. Bacon, S. Bonella, B. Rotenberg, P. A. Madden, and M. Salanne, "MetalWalls: A classical molecular dynamics software dedicated to the simulation of electrochemical systems," Journal of Open Source Software **5**, 2373–2373 (2020).

[30]A. Coretti, C. Bacon, R. Berthin, A. Serva, L. Scalfi, I. Chubak, K. Goloviznina, M. Haefele, A. Marin-Laflèche, B. Rotenberg, S. Bonella, and M. Salanne, "MetalWalls: Simulating electrochemical interfaces between polarizable electrolytes and metallic electrodes," Journal of Chemical Physics **157**, 184801–184801 (2022).

[31]K. Wendler, M. Brehm, F. Malberg, B. Kirchner, and L. Delle Site, "Short time dynamics of ionic liquids in AIMD-based power spectra," Journal of Chemical Theory and Computation **8**, 1570–1579 (2012).

[32]M. Thomas, M. Brehm, R. Fligg, P. Vöhringer, and B. Kirchner, "Computing vibrational spectra from ab initio molecular dynamics," Physical Chemistry Chemical Physics **15**, 6608–6622 (2013).

[33]A. Togo, "First-principles Phonon Calculations with Phonopy and Phono3py," Journal of the Physical Society of Japan **92**, 012001 (2022).

[34]A. Togo, L. Chaput, T. Tadano, and I. Tanaka, "Implementation strategies in phonopy and phono3py," Journal of Physics: Condensed Matter **35**, 353001–353001 (2023).

[35]K. Latimer, S. Dwaraknath, K. Mathew, D. Winston, and K. A. Persson, "Evaluation of thermodynamic equations of state across chemistry and structure in the materials project," npj Computational Materials **4**, 40 (2018).

[36]F. Birch, "Finite Elastic Strain of Cubic Crystals," Physical Review **71**, 809–824 (1947).

[37]F. D. Murnaghan, "The Compressibility of Media under Extreme Pressures," Proceedings of the National Academy of Sciences **30**, 244–247 (1944).

[38]"IDRIS - Jean Zay: HPE SGI 8600 computer," http://www.idris.fr/eng/jean-zay/index.html.